EUROPEAN ORGANIZATION FOR NUCLEAR RESEARCH

Production of K^0_S, Λ ($\overline{\Lambda}$), $\Xi^{\pm}$ and $\Omega^{\pm}$ in jets and underlying events in pp and p–Pb collisions with ALICE

ALICE Collaboration*

Abstract

The production of strange hadrons (K^0_S, Λ, $\Xi^{\pm}$ and $\Omega^{\pm}$), baryon-to-meson ratios (Λ/K^0_S, Ξ/K^0_S and Ω/K^0_S) and baryon-to-baryon ratios (Ξ/Λ, Ω/Λ and Ω/Ξ) are measured for inclusive, energetic jets and underlying events in pp collisions at $\sqrt{s}$ = 13 TeV and p–Pb collisions at $\sqrt{s_{NN}}$ = 5.02 TeV with the ALICE detector at the LHC. For the first time, we present results on multi-strange particle production and their ratios in jets and in underlying evens, providing an opportunity to test the strange particle production mechanism with a hard scattering. The transverse momentum (p_T) differential distribution of hadrons associated with jets decreases slower than the one reported for inclusive particle production. The baryon-to-meson and baryon-to-baryon ratios in jets show a clear difference when compared to the inclusive ones for both collision systems at the intermediate p_T range. On the contrary, these ratios in underlying events show the same behavior as the inclusive ones. When comparing hadron spectra and ratios within different charged-particle multiplicity bins, those in jets are found to be independent of collision multiplicity. The results provide significant evidence that the jet fragmentation is not sufficient to describe strange and multi-strange particle production in hadronic collisions at the LHC energies.

*See Appendix B for the list of collaboration members

1 Introduction

High-energy heavy-ion (A–A) collisions are expected to create, under extreme conditions of temperature and density, a deconfined state in which the degrees of freedom are partonic rather than hadronic, the Quark-Gluon Plasma (QGP) [1–7]. The structure and dynamical behavior of the QGP arise at the microscopic level from the interactions between quarks and gluons described by Quantum Chromodynamics (QCD) [8–10]. The interpretation of the heavy-ion results depends crucially on understanding results from small collision systems such as proton-proton (pp) or proton-nucleus (p-A). In p–Pb collisions, where ~~are not an~~ hot-matter effects are not expected, it is essential to investigate cold nuclear initial- and final-state effect ~~to be used~~ as the baseline for heavy-ion collisions [11, 12]. On the other hand, pp collisions constitutes a baseline for the nuclear effects in both A–A and p–A collisions. In pp collisions, there are not any hot and cold nuclear initial- and final-state effects. So it constitutes a baseline for the nuclear effects in both A–A and p-A collisions.

Several collective phenomena have been observed in high-multiplicity pp and p–Pb collisions that are reminiscent of the observation attributed to the creation of QGP in Pb–Pb collisions [13–19]. These include the long-range angular correlations on the near and away side of a trigger particle [13–15], non-vanishing 2nd order Fourier coefficients (v_2) ~~coefficients~~ in multi-particle cumulant studies [16, 17], etc. In particular, in pp and p–Pb collisions, the baryon-to-meson ratios p/π and $\Lambda/\text{K}_\text{S}^0$ manifest an enhancement at intermediate p_T (~ 3 GeV/c) [20–23] and the strange to non-strange hadron ratios show a significant enhancement with multiplicity [21, 23, 24], which is qualitatively similar to that observed in Pb–Pb collisions. On the other hand, several measurements show the absence of a robust nuclear effect on the jet production at mid-rapidity in small systems [25–33]. To understand particle production mechanisms in small collision systems, the separation of particle produced in hard processes (jet) from those of the underlying event is important. In a recent study, the ALICE Collaboration has studied baryon-to-meson ratios with a new twist: by studying the ratios in two parts of the events separately – inside jets and in the event portion perpendicular to a jet cone in pp collisions at $\sqrt{s}$ = 7 TeV and p–Pb collisions at $\sqrt{s_{\text{NN}}}$ = 5.02 TeV [34]. It is shown that the $(\Lambda + \overline{\Lambda})/2\text{K}_\text{S}^0$ ratio at intermediate p_T found in the inclusive particle measurements in Pb–Pb and high multiplicity small collision systems is not present for particles associated with hard scatterings tagged by jets. In this contribution, the baryon-to-meson ratio and multi-strange-to-strange particle ratio will be studied in charged-particle jets and underlying event. It will provide further insight into disentangle the soft process or hard scattering contributions of the baryon-to-meson ratio enhancement at intermediate p_T and the strange particle production increasing with multiplicity in small systems.

In this paper, the production of K_S^0, Λ ($\overline{\Lambda}$), $\Xi^\pm$ and $\Omega^\pm$ in charged-particle jets and underlying event in pp collisions at $\sqrt{s}$ = 13 TeV and p–Pb collisions at $\sqrt{s_{\text{NN}}}$ = 5.02 TeV is reported. Strange particles are reconstructed in the pseudo-rapidity range $|\eta| < 0.75$. Jets are reconstructed in the transverse momentum range $p_{\text{T,jet}}^{\text{ch}} > 10$ GeV/c and in the pseudo-rapidity range $|\eta| < 0.35$. The (multi-)strange particles associated with the jet are defined as a function of distance between particle momentum and jet axis in $\eta - \varphi$ plane. The results presented in this paper significantly improve the precision of the p_T-differential measurements compared to ALICE previous one [34], including also the centrality dependence and extending to the multi-strange sector in both pp (at different energy) and p–Pb collisions. The baryon-to-meson and baryon-to-baryon ratios in energetic jets are compared with the case of particles not associated with jets and PYTHIA 8 [35] simulation.

The paper is structured as follows. In Sec. 2, the ALICE apparatus and the data samples used for the analysis are presented. In Sec. 3, the methods adopted for charged-particle jet reconstruction, (multi-)strange particle reconstruction, and particle-jet matching are described. Estimated of the associated systematic uncertainties are also reported in Sec. 3. The transverse momentum dependence of (multi-)strange hadron~~s~~ distributions and particle ratios, the model comparisons, and an interpretation of the results are presented and discussed in Sec. 4.

2   ALICE detector and data selection

A detailed description of the ALICE apparatus and its performance can be found in [36, 37]. This analysis relies on the central tracking system and the forward VZERO detector [38]. The two forward scintillator arrays V0A (covering pseudo-rapidity range of $2.8 < \eta < 5.1$), and V0C ($-3.7 < \eta < -1.7$) were employed for both as triggering detectors and to determine the event multiplicity class. The main central barrel detectors used for this analysis are the Inner Tracking System (ITS) [39], the Time Projection Chamber (TPC) [40] and the Time Of Flight detector (TOF) [41–44], which cover the pseudo-rapidity region $|\eta| < 0.9$ and are located inside a large solenoidal magnet providing a 0.5 T magnetic field.

The innermost barrel detector is the ITS consisting of six cylindrical layers of high spatial resolution silicon detector using three different technologies. The two innermost layers (SPD) are based on silicon pixel technology and cover $|\eta| < 2.0$ and $|\eta| < 1.4$, respectively. The SPD was used to reconstruct the collision's primary vertex and short track segments, which are called "tracklets". The four outer ITS layers consist of silicon drift (SDD) and strip (SSD) detectors, with the outermost layer having a radius $r = 43$ cm. The SDD and SSD are able to measure the specific ionization energy loss (dE/dx) with a relative resolution around 10% in the low p_T region (up to ~ 1 GeV/c). The ITS is also used to reconstruct and identify low momentum particles down to 100 MeV/c that can not reach the TPC.

The TPC is a large cylindrical drift detector which is filled with a $Ne - CO_2$ gas mixture. The radius and the longitude dimensions of the TPC are about $85 < r < 250$ cm and $-250 < z < 250$ cm, respectively. As the main tracking device, the TPC provides full azimuthal acceptance for tracks in the pseudo-rapidity region $|\eta| < 0.9$. In addition, it provides charged-hadron identification via measurement of the specific ionization energy loss dE/dx. At low transverse momenta ($p_T \lesssim 1.0$ GeV/c), the dE/dx resolution of 5.2% for a minimum ionizing particle allows a track-by-track identification. On the other hand, at high transverse momenta ($p_T \gtrsim 2.0$ GeV/c), the overlapping energy loss has to be statistically distinguished via a multi-Gaussian fit to the dE/dx distributions.

Outside of the TPC and located at a radius of approximately 4 m, the TOF measures the particles' time of flight. The TOF is a cylindrical array of multi-gap resistive plate chambers with an intrinsic time resolution of 50 ps. It covers the pseudo-rapidity range $|\eta| < 0.9$ with full azimuthal acceptance. It can provide particle identification over a broad range at intermediate transverse momenta ($0.5 \lesssim p_T \lesssim 2.7$ GeV/c). The total time-of-flight resolution, including the collision time resolution, is about 90 ps in pp and p–Pb collisions [45, 46].

Data of pp collisions at $\sqrt{s} = 13$ TeV and of p–Pb collisions at $\sqrt{s_{NN}} = 5.02$ TeV are used in this analysis. The pp data sample was recorded in 2016–2017, the p–Pb sample in 2016 with ALICE detector, respectively. The data were collected with a minimum bias (MB) trigger requiring at least one hit in both V0 scintillators in coincidence with proton bunches' arrival from both directions. Interaction vertices are reconstructed by the extrapolation of ITS track segments towards the nominal interaction point. Pile-up events, due to multiple interactions in the triggered bunch crossing, are removed by exploiting the correlation between the number of pixel hits and the number of SPD tracklets. In addition, the coordinate of the primary vertex along the beam direction is within ± 10 cm with respect to the ALICE interaction point. After event selection, the pp sample consists of 1.5 billion events. The average number of inelastic interactions per bunch crossing ranges between 2% and 14%. The integrated luminosity of $\mathcal{L}_{int} = 9.38 \pm 0.47$ nb^{-1} based on the visible cross section observed by the V0 trigger was extracted from a van der Meer scan [47]. About 500 million events from the p–Pb samples were selected, which correspond to an integrated luminosity of $\mathcal{L}_{int} = 295 \pm 11$ μb^{-1} [48]. The p–Pb events were divided into three multiplicity classes based on the total charge deposited in the V0A (the Pb-going direction). The multiplicity intervals and their corresponding mean charged-particle density ($dN_{ch}/d\eta$) measured at mid-rapidity ($|\eta| < 0.5$) are given in Ref. [49].

3 Analysis

3.1 Charged-particle jet reconstruction

In this analysis, the FastJet package [50] is used to find jets using charged particles with the anti-k_T algorithm [51]. The anti-k_T algorithm is a commonly used jet finding algorithm which starts particle clustering from the highest momentum particles, in contrast to the k_T algorithm, which does the opposite. Charged particles, which are used as input for jet reconstruction, are reconstructed using ITS and TPC information. The charged particle tracks are selected in $|\eta_\text{trk}| < 0.9$ (TPC acceptance) and $p_\text{T} > 0.15$ GeV/c. The jet resolution parameter is $R = 0.4$ and the reconstructed jet clusters are selected in $\left|\eta_\text{jet}\right| < 0.35$. This condition ensures the jet cone is fully overlapping with the acceptances of both charged-particle tracks and the strange particles ($|\eta| < 0.75$). A $p_\text{T,jet}^\text{ch} > 10$ GeV/c cut on charged-particle jet transverse momentum, according to ALICE previous study [34] is applied, to tag the hard scattering process.

Besides the hard parton-parton interactions in the collisions, there is also the soft contribution which did not correlate with the hard collisions. The background density (ρ_bkg) determined from the k_T algorithm [52, 53] in pp collisions is around 1 GeV/c rad^{-1} and is not subtracted. In p–Pb collisions, the underlying background is larger and the reconstructed jet is therefore further corrected for contributions form the underlying event to the jet momentum as

$$p_\text{T,jet} = p_\text{T,jet}^\text{ch} - \rho_\text{bkg} \cdot A_\text{jet} \tag{1}$$

where the $p_\text{T,jet}^\text{rec}$ is the reconstructed jet p_T, A_jet is the jet area and ρ_bkg is the event-by-event background density [54]. The A_jet is calculated using the FastJet algorithm with a ghost area of 0.005 [55]. A method that is suitable for the background density estimation for sparse systems circumvents the problems arising from using the ghost jets is introduced in [56]. The basic idea is to neglect the ghosts and instead account for the empty areas by introducing a factor correcting the background density for it. It can be implemented by the following formula

$$\rho_\text{bkg} = C \cdot \text{median}\{\frac{p_\text{T,i}}{A_i}\} \text{ with } C = \frac{\sum_j A_j}{A_\text{acc}}. \tag{2}$$

Where A_j is the area of each k_T jet with at least one real track, i.e. excluding ghosts and A_acc is the area of the charged-particle acceptance, namely $(2 \times 0.8) \times 2\pi$. This method has the advantage that it uses the median and takes empty areas into account. This method can be further refined for the specific case of p–Pb collisions. It can be shown that the exclusion of the two k_T jets with highest p_T from Eq. (2) is enhancing the background quality [57, 58].

3.2 Strange particles reconstruction

The strange particles K_S^0, Λ, $\overline{\Lambda}$, $\Xi^\pm$ and $\Omega^\pm$ are reconstructed at mid-rapidity ($|\eta| < 0.75$) via their specific weak decay topology. The following decay channels are studied [59]:

$$\begin{aligned}
\text{K}_\text{S}^0 &\to \pi^+ + \pi^- & B.R. &= (69.20 \pm 0.05)\%, \\
\Lambda(\overline{\Lambda}) &\to \text{p}(\overline{\text{p}}) + \pi^-(\pi^+) & B.R. &= (63.9 \pm 0.5)\%, \\
\Xi^-(\overline{\Xi}^+) &\to \Lambda(\overline{\Lambda}) + \pi^-(\pi^+) & B.R. &= (99.887 \pm 0.035)\%, \\
\Omega^-(\overline{\Omega}^+) &\to \Lambda(\overline{\Lambda}) + \text{K}^-(\text{K}^+) & B.R. &= (67.8 \pm 0.7)\%.
\end{aligned}$$

The proton, pion, and kaon tracks (daughter tracks) are identified in the TPC via their measured energy deposition [37]. The identification of the V^0 (K_S^0 and Λ ($\overline{\Lambda}$) which decay into two oppositely charged daughter particles) and cascade ($\Xi^\pm$ and $\Omega^\pm$ which decay into a bachelor charged meson plus a V^0 decaying particle, giving the cascade decay topology) candidates follow those presented in earlier ALICE

148 publications [20, 24, 45, 60–62]. In addition, removal of contributions from pileup collisions outside the
149 trigger proton bunch ("out-of-bunch pileup"), it is achieved by requiring that at least one of the charged
150 decay track matches a hit in a "fast" detector (either the ITS or the TOF detector). The selections used in
151 this paper are summarized in Tab. A.1, A.2.

152 The signal extraction is performed as a function of p_T. In each p_T interval, an invariant mass histogram
153 is ~~produced and~~ filled with the corresponding counts. Then a Gaussian function is used to fit the peak,
154 and a linear function is used to fit the combinatorial background. This allows for the extraction of the
155 mean (μ) and width (σ) of the peak. A "peak" region is defined within $\pm 6\sigma$ for V^{0}s and $\pm 3\sigma$ ($\pm 4\sigma$)
156 for cascades in pp (and p–Pb) with respect to μ for each p_T bin. The "background" regions are defined
157 on both sides of the peak region. The p_T-differential yields of (multi-)strange particles are obtained by
158 subtraction the integral of the background fit function in the peak region from the total bin counting in
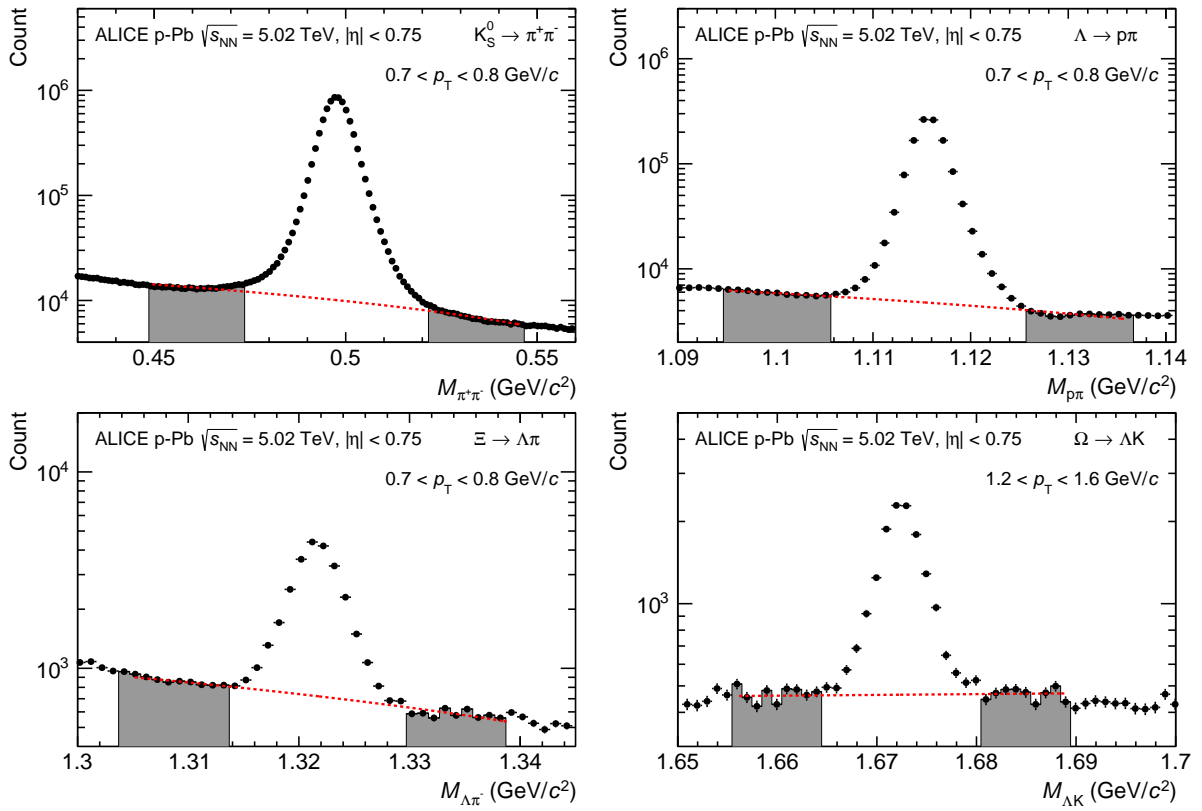   the same region. Examples of the invariant mass peaks for all particles are shown in Fig. 1.

Figure 1: Invariant mass distribution for K^0_S, Λ, Ξ and Ω in different p_T intervals in MB p–Pb collisions at
$\sqrt{s_{NN}}$ = 5.02 TeV. The candidates are reconstructed in $|\eta| < 0.75$. The grey areas are used for background
estimation applied in the signal extraction in the bin counting procedure.

159

3.3 Matching of strange particles to jets and underlying event

161 The strategy of matching the (multi-)strange particles with jets follow those presented in earlier work [34].
162 The matching is done on a geometrical basis according to the distance variable defined in Eq. 3.

$$d(\text{particle}, \text{jet}) = \sqrt{(\eta_{\text{particle}} - \eta_{\text{jet}})^2 + (\varphi_{\text{particle}} - \varphi_{\text{jet}})^2} \qquad (3)$$

163 If the distance between the particle candidate and the jet (d) is smaller than a pre-defined maximum
164 distance ($D_{\text{max}} = 0.4$), the candidate is considered to be inside the jet cone (JC). The raw yields in JC

are not only composed of the hadrons produced via jet fragmentation (JE), but also from hadrons from the underlying event (UE) defined as the sum of all particles which are not produced via hard parton fragmentation. The UE contribution is estimated by perpendicular cone (PC) yields. The PC indicates the cone in the $\eta-\varphi$ space located at the perpendicular direction with respect to the jet axis at the same η. In addition, the acceptance selections of inclusive (regardless of the association between the particle and hard scattering), JC and UE (multi-)strange particles are different in the $\eta-\varphi$ plane. To estimate the contribution from JE the p_{T}-differential particle density ($\mathrm{d}\rho/\mathrm{d}p_{\mathrm{T}}$) is defined in:

$$
\begin{aligned}
\text{Inclusive}: \quad & \frac{\mathrm{d}\rho}{\mathrm{d}p_{\mathrm{T}}} = \frac{1}{N_{\mathrm{ev}}} \times \frac{1}{\Delta\eta\Delta\varphi} \times \frac{\mathrm{d}N}{\mathrm{d}p_{\mathrm{T}}}, \\
\text{JC}: \quad & \frac{\mathrm{d}\rho}{\mathrm{d}p_{\mathrm{T}}} = \frac{1}{N_{\mathrm{ev}}^{\mathrm{jet}}} \times \frac{1}{A_{\mathrm{jet}}} \times \frac{\mathrm{d}N}{\mathrm{d}p_{\mathrm{T}}}, \\
\text{PC}: \quad & \frac{\mathrm{d}\rho}{\mathrm{d}p_{\mathrm{T}}} = \frac{1}{N_{\mathrm{ev}}^{\mathrm{jet}}} \times \frac{1}{A_{\mathrm{PC}}} \times \frac{\mathrm{d}N}{\mathrm{d}p_{\mathrm{T}}}.
\end{aligned}
\tag{4}
$$

Where the $\Delta\eta\Delta\varphi$ is the acceptance in pseudo-rapidity and azimuthal angle, the A_{jet} is the jet area, and the A_{PC} is the perpendicular cone area. The density of particles within jet (JE) can be defined as:

$$
\mathrm{JE} = \mathrm{JC} - \mathrm{PC}.
\tag{5}
$$

3.4 Corrections for strange particles reconstruction and feed-down

The reconstruction efficiency of each particle is obtained from Monte Carlo simulated data. For this purpose PYTHIA 8.2 [35] and DPMJet [63] in pp and p–Pb collisions are used and the simulated data are propagated through the detector by GEANT 3 [64] to simulate ALICE detector response. Due to differences in the experimental acceptance for particles associated with jets and underlying event, the efficiencies of particles are estimated separately for every case [34]. Fig. 2 shows the difference of reconstruction efficiency of JC particle yields and the inclusive one.
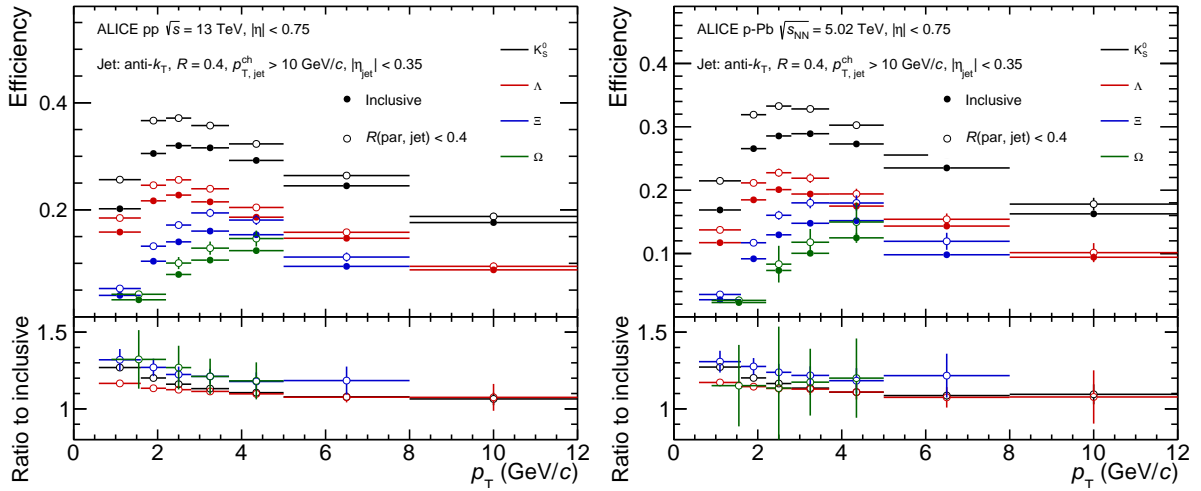

Figure 2: Strange particle reconstruction efficiency in pp collisions at $\sqrt{s} = 13$ TeV (left) and in p–Pb collisions at $\sqrt{s_{\mathrm{NN}}} = 5.02$ TeV (right) for two selections: inside jet cone, $R(\mathrm{par},\mathrm{jet}) < 0.4$ and the inclusive one.

Only the yields for Λ and $\overline{\Lambda}$ are significantly affected by secondary particles coming from the decays of charged and neutral Ξ baryons. The feed-down fraction is calculated with a data-driven approach [24]. The detailed of inclusive feed-down method have been introduced in previous ALICE analyses [23, 45, 62]. In particular, the Λ and $\overline{\Lambda}$ in jet and UE feed-down component is usually estimated by inclusive $\Xi^{\pm}$

spectra and PYTHIA simulations [34], due to lack of $\Xi^{\pm}$ in jet and UE results. In this work, the feed-down fraction in jets and UE is computed for each p_T bin by the measured $\Xi^{\pm}$ in jets and UE spectra, thereby assuming that the production rates of charged and neutral Ξ are equal. Figure 3 shows the results of feed-down fraction in JC and the inclusive one.
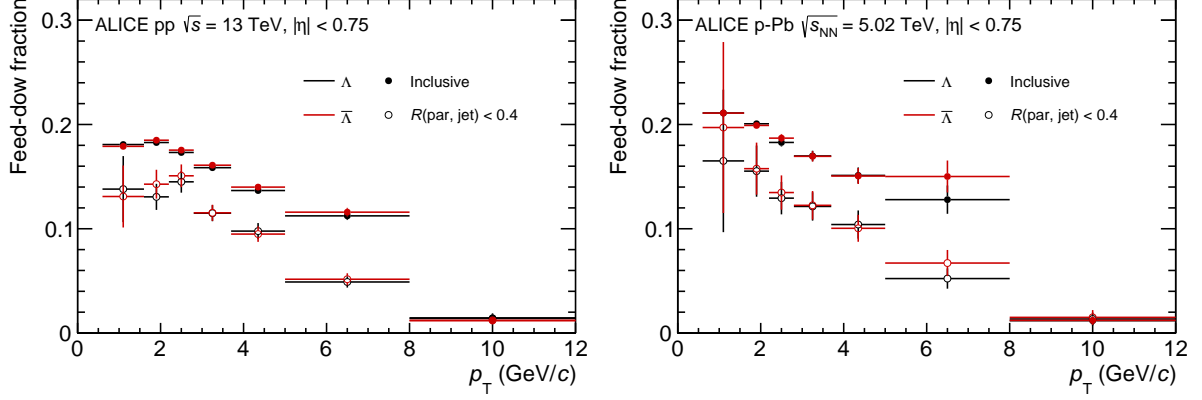

Figure 3: Fraction of Λ spectra removed due to feed-down subtraction of charged and neutral Ξ

3.5 Systematic uncertainties

Total systematic uncertainty, for K_S^0, Λ, $\overline{\Lambda}$, $\Xi^{\pm}$ and $\Omega^{\pm}$ yields have been estimated separately in each p_T interval. Individual settings are loosened and tightened, in order to measure changes in the signal loss correction. The main sources of the systematic uncertainty in this measurements are related to the knowledge of detector materials, track selections, particle identification, proper lifetime, topological selection and signal extraction. All these individual error contributions, which are listed in Tab. 1, 2 are added in quadrature.

Table 1: Main sources and values of the relative systematic uncertainties (%) of K_S^0, $\Lambda + \overline{\Lambda}$, $\Xi^- + \overline{\Xi}^+$ and $\Omega^- + \overline{\Omega}^+$ in pp collisions at $\sqrt{s} = 13$ TeV. The values are reported for low, intermediate and high p_T.

Uncertainty source	K_S^0			$\Lambda + \overline{\Lambda}$			$\Xi^- + \overline{\Xi}^+$			$\Omega^- + \overline{\Omega}^+$		
p_T (GeV/c)	0.6	2	10	0.6	2	10	0.6	2	7	1	2	5
Detector material	4	4	4	4	4	4	4	4	4	4	4	4
Track selection	1.5	1.2	0.4	0.6	1.4	1.3	2.8	0.1	0.	0.	1.5	0.2
Particle identification	0.1	0.1	0.1	0.3	0.2	1.1	1.9	1.7	2.4	3.9	8.7	6.
Proper lifetime	0	0.1	0	2.1	0.4	0	-	-	-	-	-	-
Topological	0.2	1.4	0	3.9	0.8	3.9	0.6	0.9	1.	2.8	5.4	2.4
Signal extraction	0.8	1.1	1.1	0.3	0.5	1.7	3.	1.	0.5	2.3	4.6	3
Total uncertainty	4.4	4.6	4.2	6.1	4.4	6.1	6.1	4.5	4.8	6.7	12.	8.2

Material budget. The effect of the incomplete knowledge of the detector's material budget is evaluated by comparing different Monte Carlo simulations in which the material budget was increased and decreased by 4.5%. This value corresponds to the uncertainty on the determination of the material budget by measuring photon conversions [37]. This particular systematic uncertainty is around 4% [45].

Track selection. To estimate the systematic uncertainty due to the track selection, the analysis has been redone with an increased number of required clusters in the TPC from default 70 points to 80 points.

Table 2: Main sources and values of the relative systematic uncertainties (%) of K_S^0, $\Lambda + \overline{\Lambda}$, $\Xi^- + \overline{\Xi}^+$ and $\Omega^- + \overline{\Omega}^+$ in p–Pb collisions at $\sqrt{s_{NN}} = 5.02$ TeV. The values are reported for low, intermediate and high p_T values.

Uncertainty source	K_S^0			$\Lambda + \overline{\Lambda}$			$\Xi^- + \overline{\Xi}^+$			$\Omega^- + \overline{\Omega}^+$		
p_T (GeV/c)	0.6	2	10	0.6	2	10	0.6	2	7	1	2	5
Detector material	0.4	0.4	0.4	0.4	0.4	0.4	0.4	0.4	0.4	0.4	0.4	0.4
Track selection	1.4	1.7	1.8	0.2	1.3	1.4	0	0	0	1.3	2.5	0
Particle identification	0.1	0.2	0.2	0.3	0.2	1	3.1	1.2	0	8.1	13.7	5.9
Proper lifetime	0	0	0	1.6	0.3	0	0.6	0.4	0	0	3.3	0
Topological	4.4	0.6	1.9	3.9	0.9	2.7	1.3	0	2.6	1.2	4.8	3.7
Signal extraction	0.3	2.6	1.7	0.6	0.5	2.6	5.1	0.9	2.6	0	5.2	0
Total uncertainty	6.1	5.1	5.1	5.8	4.3	5.8	7.4	4.3	5.4	9.2	16.4	8

Particle identification. The TPC dE/dx selection is used to reduce the combinatorial background in the (multi-)strange particle invariant mass distribution. The number of Gaussian σ in the identification of particles using the dE/dx has been varied from 4σ to 6σ.

Proper lifetime selection. The proper lifetime is defined as mLc/p, where m is the mass of the particles, L is the decay length, and p is the particle's momentum. The selection on the mLc/p is varied within 12 to 40 cm for K_S^0, 20 to 40 cm for Λ ($\overline{\Lambda}$), 10 to 30 cm for $\Xi^\pm$, and 5 to 15 cm $\Omega^\pm$.

Topological selection. The values of the selection criteria for the topological variables are varied within ranges leading to a maximum variation of $\pm 10\%$ in the raw singal yied around their nominal values. The observed deviations for each component are summed in quadrature.

Signal extraction. In the same spirit, the signal extraction technique has been tested by varying the widths used to define the "signal" and "background" regions, expressed in terms of the number of σ as defined in Sec. 3.2. In particular the width of the peak region has been varied from the standard 6σ to 7σ, 5σ and 4σ for V^0 particles and 3σ to 4σ (3.5σ) and 2.5σ for $\Xi(\Omega)$.

The additional systematic uncertainty sources associated with particle yield in the jet originate from the UE subtraction estimator and the jet p_T threshold. The systematic uncertainty due to the UE subtraction is estimated by varying the perpendicular cone radius from the chosen thresholds of 0.4 (PC04) to 0.2 (PC02) and 0.6 (PC06). From the deviations obtained for different PC cone size, the relative systematic uncertainty of the UE subtraction is estimated. To estimate the effect of jet p_T threshold uncertainty, the analysis is repeated with the jet p_T cut 10 ± 1 GeV/c. The systematic uncertainties of particles in jets are added to the list of uncertainties in quadrature. The values are shown in Table 3, 4.

The uncertainties of jet cone particle ratios (Λ/K_S^0, Ξ/K_S^0, Ω/K_S^0, Ξ/Λ, Ω/Λ and Ω/Ξ) also include three sources: the particle reconstruction, UE subtraction and the jet p_T threshold. The particle reconstruction uncertainty is propagated from the particle spectra. Uncertainties related to UE subtraction and jet p_T threshold are obtained by varying the same condition as particle spectra in both numerator and denominator of the corresponding ratios.

Table 3: Main sources and values of the relative systematic uncertainties (%) of particle p_T-differential density (K_S^0, $\Lambda+\overline{\Lambda}$, $\Xi^-+\overline{\Xi}^+$ and $\Omega^-+\overline{\Omega}^+$) and particle ratios ($\Lambda/K_S^0$, Ξ/K_S^0, Ω/K_S^0, Ξ/Λ, Ω/Λ and Ω/Ξ) in JE in pp collisions at $\sqrt{s} = 13$ TeV. The values are reported for low, intermediate and high p_T.

Uncertainty source	K_S^0			$\Lambda+\overline{\Lambda}$			$\Xi^-+\overline{\Xi}^+$			$\Omega^-+\overline{\Omega}^+$		
p_T (GeV/c)	0.6	2	10	0.6	2	10	0.6	2	7	1	2	5
Particle reconstruction	1.8	0.25	0.1	5.3	0.6	0	6.7	0.9	0.1	6	1.7	0.3
UE subtraction	0.1	0.1	0.1	0.1	0.2	0.1	1.5	0.2	0.3	3.6	1.8	0.5
Jet p_T threshold	0.6	3,1	10.9	0.6	1.1	9.9	3.5	2.4	5	0	0	0
Total uncertainty	1.8	3.1	10.9	5.3	1.2	9.9	7.7	2.6	5	7.1	2.5	0.6

Uncertainty source	$(\Lambda+\overline{\Lambda})/(2K_S^0)$			$(\Xi^-+\overline{\Xi}^+)/(2K_S^0)$			$(\Omega^-+\overline{\Omega}^+)/(2K_S^0)$		
p_T (GeV/c)	0.6	2	10	0.6	2	7	1	2	5
Particle reconstruction	2.4	2.8	2.5	3.4	2.8	2.8	6.7	11.4	7.3
UE subtraction	0.8	0.2	0.4	3.5	0.2	0.1	10	4	2.2
Jet p_T threshold	0.4	2.3	1	1.7	1.6	3.6	1.	3.3	6.4
Total uncertainty	2.6	3.7	2.7	5.2	3.3	4.5	12.4	12.5	10

Uncertainty source	$(\Xi^-+\overline{\Xi}^+)/(\Lambda+\overline{\Lambda})$			$(\Omega^-+\overline{\Omega}^+)/(\Lambda+\overline{\Lambda})$			$(\Omega^-+\overline{\Omega}^+)/(\Xi^-+\overline{\Xi}^+)$		
p_T (GeV/c)	0.6	2	7	1	2	5	1	2	5
Particle reconstruction	3.4	3	3.2	6.7	11.5	7.5	6.8	11.5	7.4
UE subtraction	4.4	0.4	0.2	12.4	4.2	2.3	7.8	3.8	2.7
Jet p_T threshold	0.7	0.5	1.9	0.2	0.9	3.5	0.4	1.3	3
Total uncertainty	5.6	3	3.7	14.1	12.2	8.6	10.3	12.1	8.5

Table 4: Main sources and values of the relative systematic uncertainties (%) of particle p_T-differential density (K_S^0, $\Lambda + \overline{\Lambda}$, $\Xi^- + \overline{\Xi}^+$ and $\Omega^- + \overline{\Omega}^+$) and particle ratios ($\Lambda/K_S^0$, Ξ/K_S^0, Ω/K_S^0, Ξ/Λ, Ω/Λ and Ω/Ξ) in JE in p–Pb collisions at $\sqrt{s_{NN}}$ = 5.02 TeV. The values are reported for low, intermediate and high p_T.

Uncertainty source	K_S^0			$\Lambda + \overline{\Lambda}$			$\Xi^- + \overline{\Xi}^+$			$\Omega^- + \overline{\Omega}^+$		
p_T (GeV/c)	0.6	2	10	0.6	2	10	0.6	2	7	1	2	5
Particle reconstruction	5	0.8	0	13.2	1.5	0	24.8	2.8	0.3	8.7	3.7	0.9
UE subtraction	0.3	0.1	0.1	0	0.1	11.2	14.1	0.8	0.7	0	0	1.2
Jet p_T threshold	0.3	3.5	11	3.2	1.8	0.1	24.9	3	4.1	3.1	10.7	7.6
Total uncertainty	5	3.6	11	13.5	2.3	11.2	37.9	4.2	4.1	9.3	11.3	7.7

Uncertainty source	$(\Lambda + \overline{\Lambda})/(2K_S^0)$			$(\Xi^- + \overline{\Xi}^+)/(2K_S^0)$			$(\Omega^- + \overline{\Omega}^+)/(2K_S^0)$		
p_T (GeV/c)	0.6	2	10	0.6	2	7	1	2	5
Particle reconstruction	3.2	3.4	3.3	4.7	3.2	4	9.8	1.5	7.4
UE subtraction	0.8	0.1	0.1	9.1	1.8	1	4.1	0	0.3
Jet p_T threshold	1.4	2.6	0.1	8.6	2.4	6	0.5	1.5	0.3
Total uncertainty	3.6	4.3	3.3	13.4	4.4	7.2	10.6	15.1	7.4

Uncertainty source	$(\Xi^- + \overline{\Xi}^+)/(\Lambda + \overline{\Lambda})$			$(\Omega^- + \overline{\Omega}^+)/(\Lambda + \overline{\Lambda})$			$(\Omega^- + \overline{\Omega}^+)/(\Xi^- + \overline{\Xi}^+)$		
p_T (GeV/c)	0.6	2	10	0.6	2	7	1	2	5
Particle reconstruction	4.1	2.8	3.7	9.6	15	7.5	10	14.9	8.6
UE subtraction	9.9	1.9	0.8	3.6	0.1	0.3	11	1.8	0.1
Jet p_T threshold	2.7	0.6	2.6	0.4	5	3	0.4	3.8	1.7
Total uncertainty	11.1	3.4	4.6	10.3	15.8	8.1	14.9	15.5	8.7

4 Results and discussion

4.1 Particles p_T-differential density

For the strange hadrons discussed in this paper, the ratios of yields for particles and anti-particles are around one within the uncertainties, as expected at these collision energies in the mid-rapidity region [45, 65]. Therefore, all the p_T-differential densities are reported after summing over particle and anti-particles. The different selections shown below have been introduced in Sec. 3.3, in which also normalization method has been introduced.
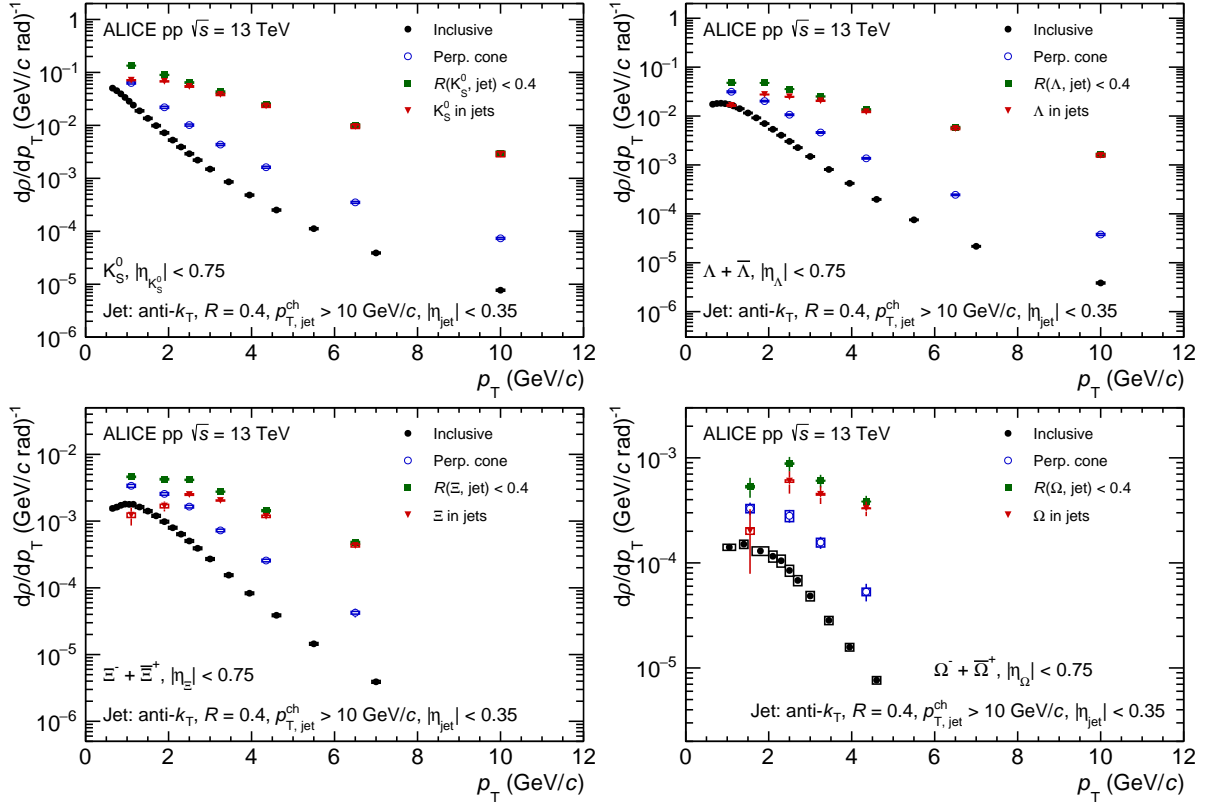
Figure 4: p_T-differential density of K_S^0, $\Lambda + \overline{\Lambda}$, $\Xi^- + \overline{\Xi}^+$ and $\Omega^- + \overline{\Omega}^+$ in pp collisions at $\sqrt{s} = 13$ TeV. The black points represent particles from minimum bias events, the green points represent particles from the jet cones, the blue points represent particles within a cone perpendicular to the jet, associated with the underlying event and the red points represent the particle from the jet fragmentation.

The fully corrected p_T-differential densities ($\mathrm{d}\rho/\mathrm{d}p_T$ defined by Eq. 4), for K_S^0, $\Lambda + \overline{\Lambda}$, $\Xi^- + \overline{\Xi}^+$ and $\Omega^- + \overline{\Omega}^+$, in pp and MB p–Pb collisions are shown in Fig. 4 and 5, respectively. The p_T-differential particle density ($\mathrm{d}\rho/\mathrm{d}p_T$) within charged-particle jets is compared with that of inclusive particles and with perpendicular cone particles. As expected the p_T dependence of the density of those hadrons within jets,as defined in Eq. 5, is considerably less steep than in the case of inclusive particles. The p_T-differential density distribution of inclusive hadrons is lower than that of the PC selection since the latter are obtained from events contain jets with $p_{T,\mathrm{jet}}^{\mathrm{ch}} > 10$ GeV/c. At the high-p_T ($p_T > 4$ GeV/c) region, the density of particle within charged-particle jets is consistent with the one in jet cone (without the underlying event subtraction). This is consistent with the expectation that the high-p_T particles originate from jet fragmentation.

In the previous studies of ALICE experiment [65–67], the stronger multiplicity dependence of the inclusive p_T-differential spectra shapes of heavier particles is observed. It also a important evidence for
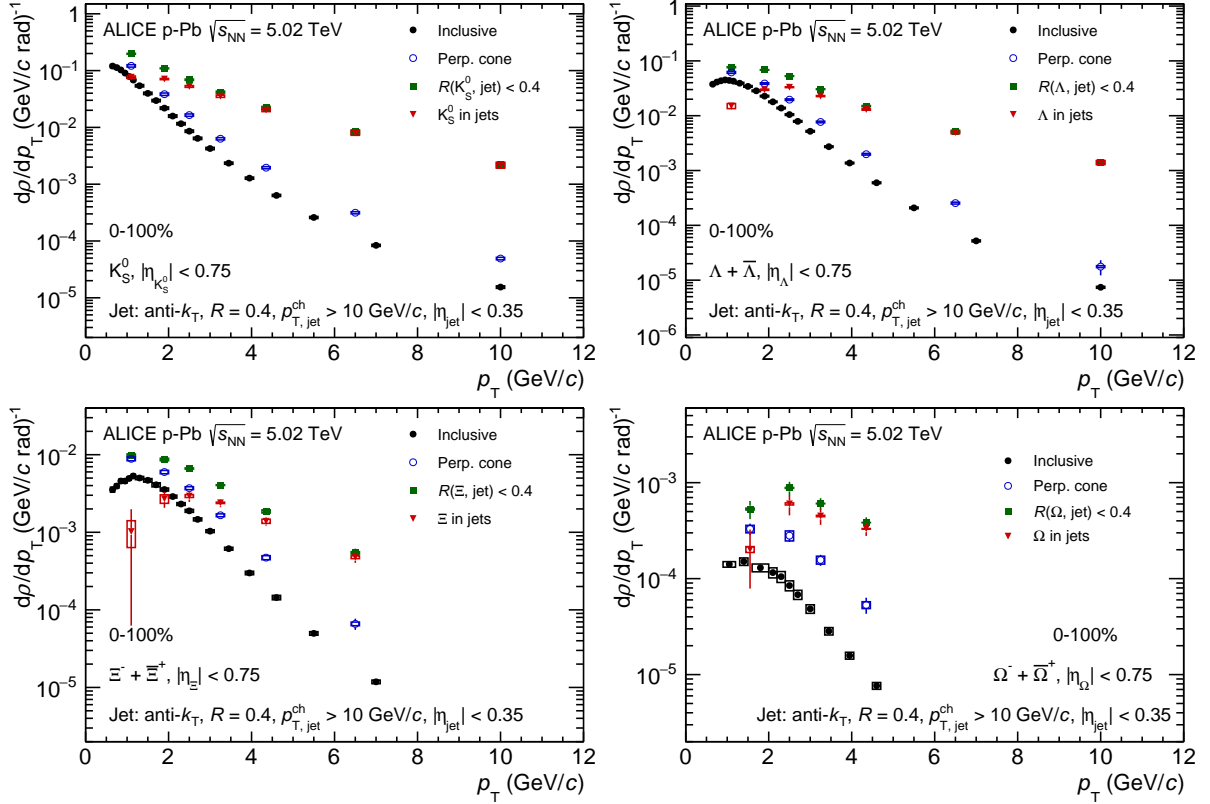
11

Figure 5: p_T-differential density of K_S^0, $\Lambda + \overline{\Lambda}$, $\Xi^- + \overline{\Xi}^+$ and $\Omega^- + \overline{\Omega}^+$ in 0-100% in p–Pb at $\sqrt{s_{NN}}$ = 5.02 TeV. The black points represent particles from minimum bias events, the green points represent particles from the jet cones, the blue points represent particles within a cone perpendicular to the jet, associated with the underlying event and the red points represent the particle from the jet fragmentation.

the baryon-to-meson ratio enhancement at intermediate-p_T. The p_T-differential densities distributions of K_S^0, $\Lambda + \overline{\Lambda}$, $\Xi^- + \overline{\Xi}^+$ and $\Omega^- + \overline{\Omega}^+$ particles within jet are shown in Fig. 6 for different charged-particle multiplicity bins. The bottom panels depict the ratio to the minimum bias (0-100%) p_T distribution. For the $\Omega^- + \overline{\Omega}^+$ in jet density, only the minimum bias distribution is shown. These spectra are compared to the particles in charged-particle jets with PYTHIA 8 simulation with Monash tune. The PYTHIA 8 can describe the K_S^0 and $\Lambda + \overline{\Lambda}$ well, but not for the $\Xi^- + \overline{\Xi}^+$ and $\Omega^- + \overline{\Omega}^+$. In Fig. 6, the K_S^0, $\Lambda + \overline{\Lambda}$ and $\Xi^- + \overline{\Xi}^+$ particle p_T spectra do not show any dependent on the charged-particle multiplicity which observed in that of inclusive particles [65–67]. Then the particle associated with jet fragmentation process may not contribute on the baryon-to-meson ratio enhancement in high multiplicity INEL events with respect to that in lower multiplicity events in small collision systems.
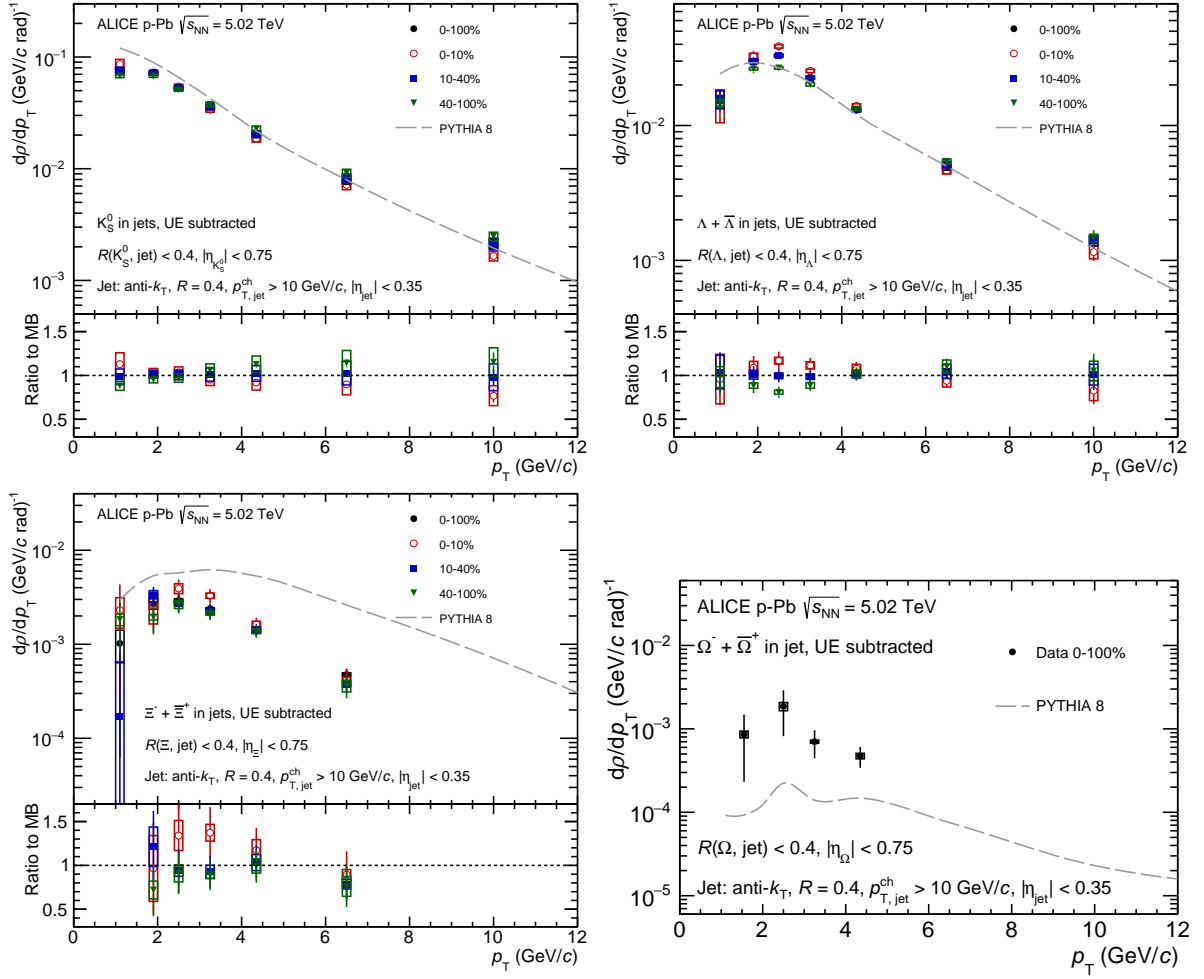
Figure 6: p_{T}-differential density of K_S^0, $\Lambda + \overline{\Lambda}$, $\Xi^- + \overline{\Xi}^+$ and $\Omega^- + \overline{\Omega}^+$ (0-100% only) particles within jets in different V0A event multiplicity classes in p–Pb collisions at $\sqrt{s_{\mathrm{NN}}} = 5.02$ TeV. The different centrality classes are depicted with different color. In the bottom panels ratios of multiplicity dependent spectra to minimum bias are shown. The systematic uncertainties on the ratios are obtained by considering only contributions uncorrelated across multiplicity. The dashed curves represent PYTHIA 8 simulations to the measured spectra.

4.2 Baryon-to-meson and baryon-to-baryon ratios

The $(\Lambda + \overline{\Lambda})/2K_S^0$, $(\Xi^- + \overline{\Xi}^+)/2K_S^0$ and $(\Omega^- + \overline{\Omega}^+)/2K_S^0$ baryon-to-meson ratios and $(\Xi^- + \overline{\Xi}^+)/(\Lambda + \overline{\Lambda})$, $(\Omega^- + \overline{\Omega}^+)/(\Lambda + \overline{\Lambda})$ and $(\Omega^- + \overline{\Omega}^+)/(\Xi^- + \overline{\Xi}^+)$ baryon-to-baryon ratios can be obtained by dividing the normalized density distributions. This ratios are investigated as a function of p_T for several selections which are introduced in Sec. 3.3 in pp and p–Pb collisions. As can be seen in Fig. 7 (pp collisions at $\sqrt{s} = 13$ TeV) and Fig. 8 (p–Pb collisions at $\sqrt{s_{NN}} = 5.02$ TeV, 0-100%), the inclusive and the PC particle ratio distributions manifest an enhancement at $p_T \sim 3 - 4$ GeV/c. The measurement of the inclusive case differs from that in Ref. [65–67] as the region $|\eta_{lab}| < 0.75$ is used here instead of the rapidity region in centre-of-mass frame $0 < y_{CMS} < 0.5$. The measurement is ortherwise consistent with them. The ratios within charged-particle jets are significantly lower than those for the inclusive and UE case at low and intermediate p_T. Also the ratios in jet are approximately independent of p_T beyond 2 GeV/c. This suggests that the ratios of baryon-to-meson and baryon-to-baryon enhancement at intermediate p_T is not driven by the jet fragmentation.

Fig. 9 shows the particle ratios in jet in pp collisions and in the different multiplicity classes in p–Pb collisions for the same selection of the matching radius $R(\text{particle,jet}) < 0.4$ in both systems. The systematic uncertainties (open boxes) are uncorrelated between the systems. The particle ratios in the jet are observed to be relatively multiplicity class and system independent. It is noteworthy that the baryon-to-meson (Λ/K_S^0, Ξ/K_S^0 and Ω/K_S^0) ratios have a hint of multiplicity (collision system) dependence for $2 < p_T < 4$ GeV/c, however the difference between the ratios is less than 2σ and the measurement is currently dominated by large uncertainties. For $p_T > 5$ GeV/c, the baryon-to-meson ratios become consistent for all multiplicity classes and collision systems. In the Fig 9, these ratios are compared to the PYTHIA 8 simulation with Monash tune. Due to the PYTHIA overestimate with $(\Xi^- + \overline{\Xi}^+)$ (see Fig. 6) in jet spectra. So here we observed the PYTHIA can simulate the $(\Lambda + \overline{\Lambda})/2K_S^0$ well but not for the ratios which correlated with multi-strange particles.
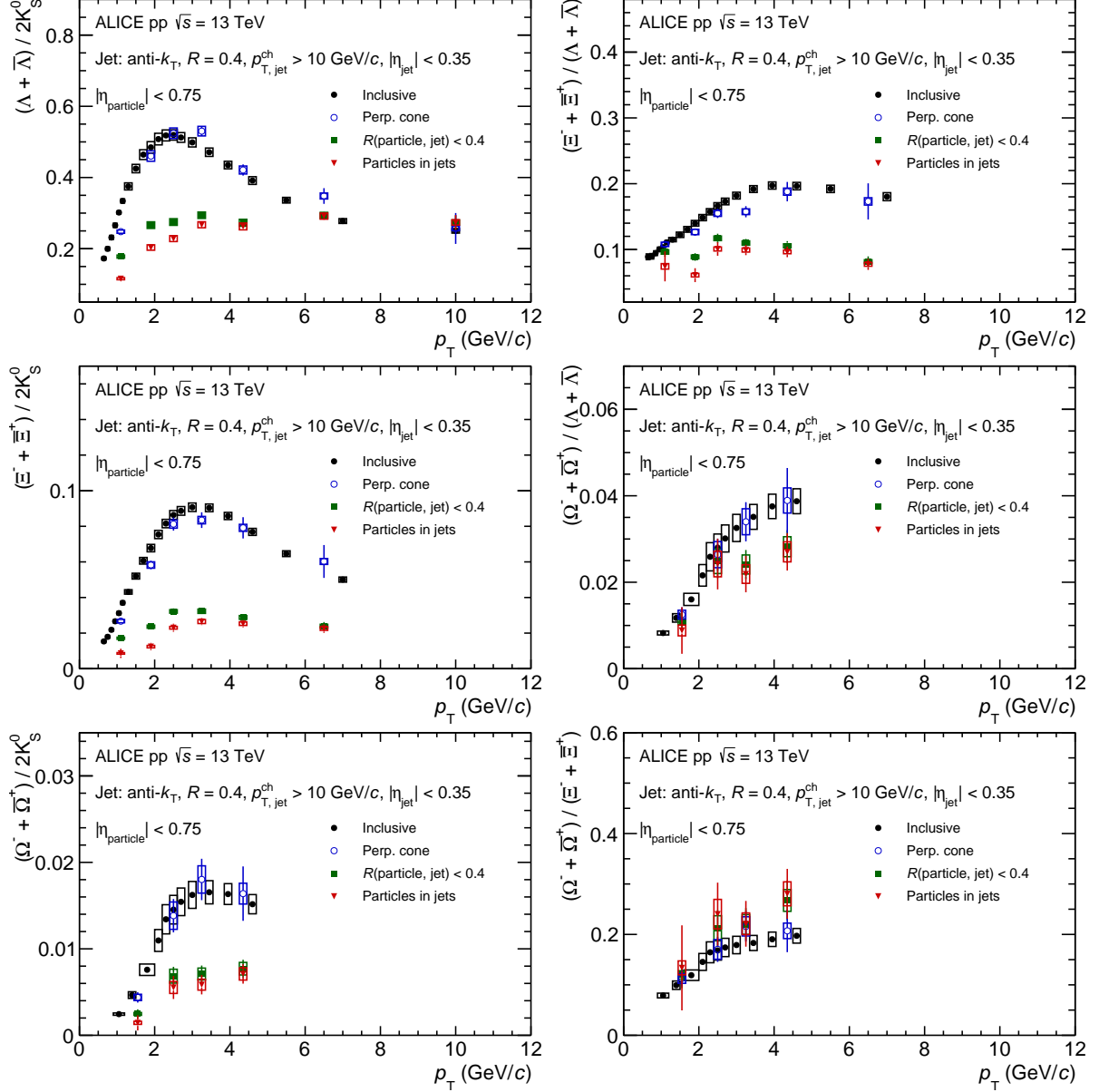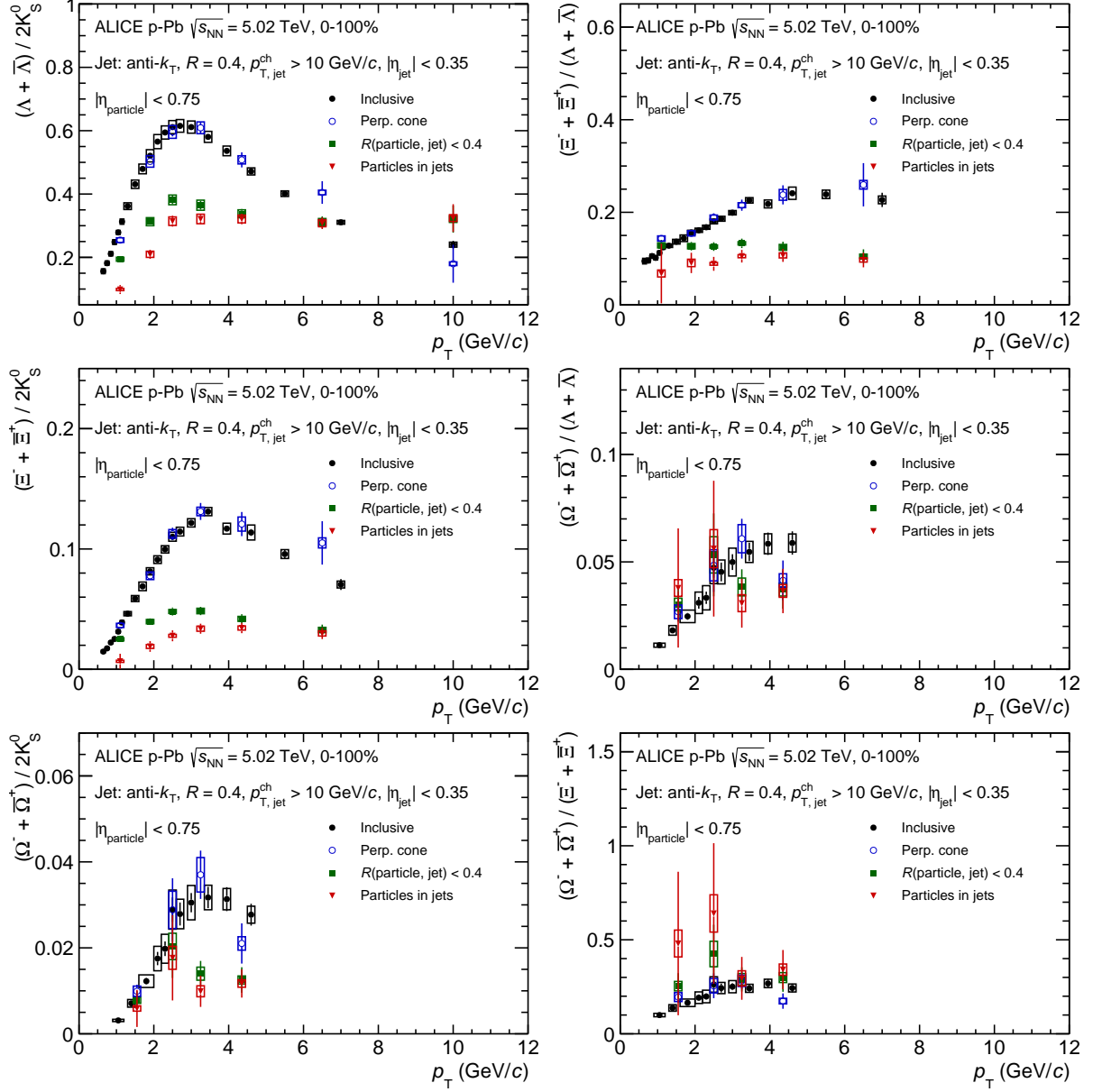
Figure 7: The baryon-to-meson (left) and baryon-to-baryon (right) ratio as a function of particle p_T in pp collisions at $\sqrt{s}$ = 13 TeV. The black points correspond to the ratio with particles from minimum bias events, the green points correspond to the ratio with particles from the jet cones, the blue points correspond to the ratio with particles ratio within a cone perpendicular to the jet, associated with the underlying event and the red points represent the ratio from the jet fragmentation. Charged-particle jets with $p_{T,jet}^{ch} > 10$ GeV/c were reconstructed with the anti-k_T algorithm with $R = 0.4$.
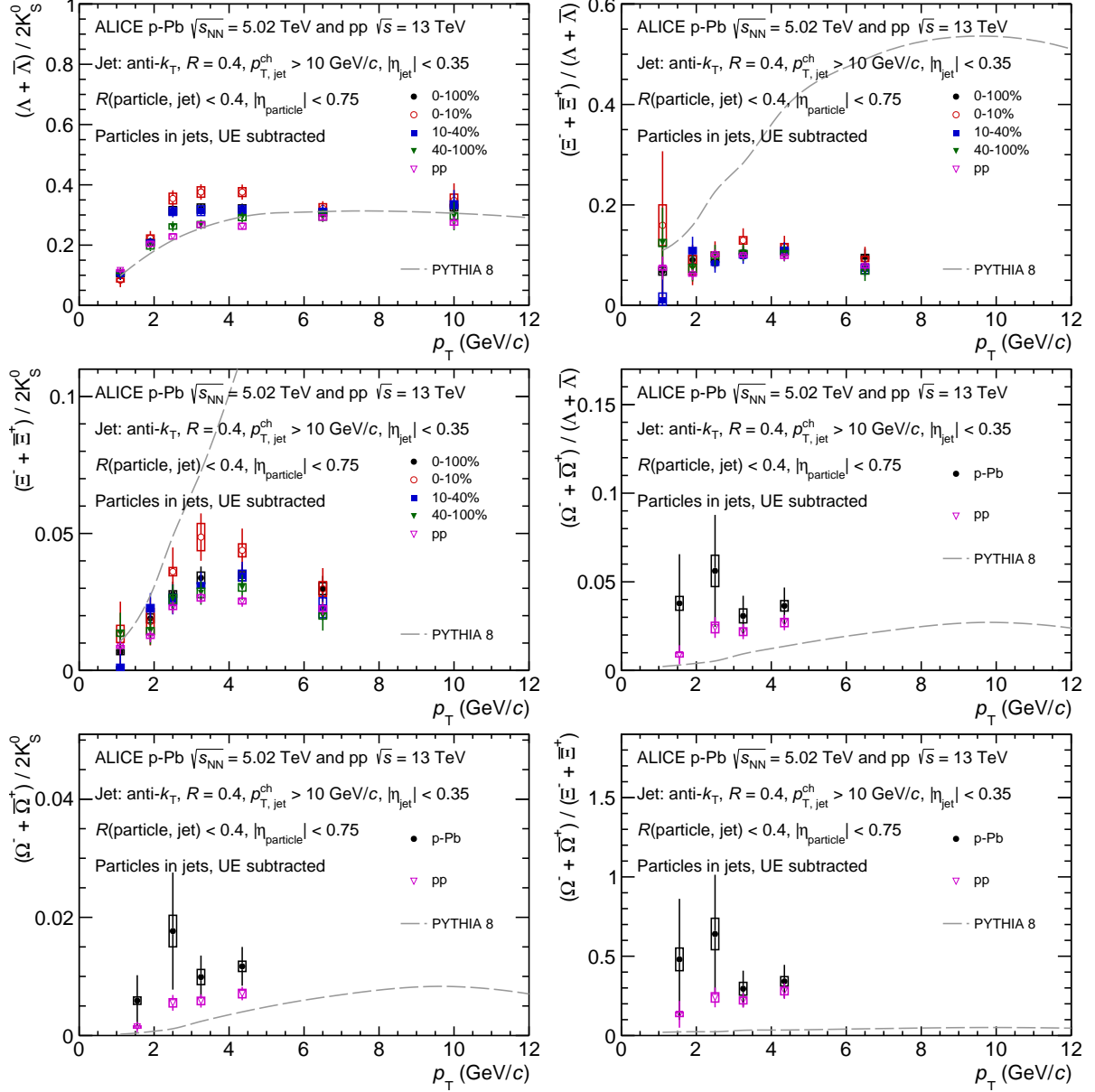
Figure 8: The baryon-to-meson (left) and baryon-to-baryon (right) ratio as a function of particle p_T in p–Pb collisions at $\sqrt{s_{NN}} = 5.02$ TeV. The black points correspond to the ratio with particles from minimum bias events, the green points correspond to the ratio with particles from the jet cones, the blue points correspond to the ratio with particles ratio within a cone perpendicular to the jet, associated with the underlying event and the red points represent the ratio from the jet fragmentation. Charged-particle jets with $p_{T,jet}^{ch} > 10$ GeV/c were reconstructed with the anti-k_T algorithm with $R = 0.4$.

Figure 9: The baryon-to-meson (left) and baryon-to-baryon (right) ratio in pp (open symbols) collisions at $\sqrt{s}$ = 13 TeV and p–Pb (full symbols) collisions at $\sqrt{s_{NN}}$ = 5.02 TeV as a function of particle p_T associated with charged particle jets with $p_{T,jet}^{ch}$ > 10 GeV/c reconstructed using the anti-k_T jet finder with resolution parameter $R = 0.4$. The ratios are shown for the same selection of the matching radius R(particle, jet) < 0.4 in both systems. The different centrality classes for p–Pb collisions are depicted with different color. The dashed curves represent PYTHIA 8 simulations to the measured ratios

5   Summary

The first measurement of the K_S^0, Λ ($\overline{\Lambda}$), $\Xi^{\pm}$ and $\Omega^{\pm}$ p_T-differential density, the Λ/K_S^0, Ξ/K_S^0 and Ω/K_S^0 baryon-to-meson ratio and the Ξ/Λ, Ω/Λ and Ω/Ξ baryon-to-baryon ratio in charged-particle jets and underlying events in pp collisions at $\sqrt{s} = 13$ TeV and p–Pb collisions at $\sqrt{s_{NN}} = 5.02$ TeV have been studied. All the measured quantities are compared with PYTHIA 8 model predictions. The PYTHIA 8 with the standard Monash trigg tune can describe the K_S^0, $\Lambda + \overline{\Lambda}$, but not for the $\Xi^- + \overline{\Xi}^+$ and $\Omega^- + \overline{\Omega}^+$. The main aim of the presented analysis, based on charged-particle jet to separate hard and soft process, is to provide insight into the understanding of the origin of flow-like correlations observed in small systems.

For all particle the p_T-differential density in events with charged-particle jet ($p_{T,jet}^{ch} > 10$ GeV/c) are observed to be harder than that in MB events. In addition, the dependence on charged-particle multiplicity found in the inclusive particle is not present for particles generated by jet fragmentation. The baryon-to-meson and baryon-to-baryon ratios associated with jets in p–Pb collisions for $R(\text{particle,jet} < 0.4)$ is consistent with the ratio measured in pp collisions. The ratios are observed to be independent on the multiplicity class of p–Pb collisions. The enhancement of baryon-to-meson ratio at intermediate p_T found in the inclusive particle are not present for particles associated with hard scattering tagged by jets reconstructed from charged particles for $p_{T,jet}^{ch} > 10$ GeV/c in pp and p–Pb collisions. Moreover, as the baryon-to-meson enhancement has been linked to the interplay of radial flow and parton recombination at intermediate p_T, its absence within the jet cone demonstrates that these effects are indeed limited to the soft particle production process.

Acknowledgements

References

[1] J. Rafelski and R. Hagedorn, "From hadron gas to quark matter, 2",.
https://cds.cern.ch/record/126179.

[2] H. Satz, "Color deconfinement in nuclear collisions", *Rept. Prog. Phys.* **63** (2000) ,
arXiv:hep-ph/0007069.

[3] E. V. Shuryak, "Theory and phenomenology of the QCD vacuum", *Phys. Rept.* **115** (1984) .

[4] B. V. Jacak and B. Muller, "The exploration of hot nuclear matter", *Science* **337** (2012) .

[5] J. Cleymans, R. Gavai, and E. Suhonen, "Quarks and Gluons at High Temperatures and
Densities", *Phys. Rept.* **130** (1986) .

[6] S. Bass, M. Gyulassy, H. Stoecker, and W. Greiner, "Signatures of quark gluon plasma formation
in high-energy heavy ion collisions: A Critical review", *J. Phys. G* **25** (1999) ,
arXiv:hep-ph/9810281.

[7] P. Braun-Munzinger and J. Stachel, "The quest for the quark-gluon plasma", *Nature* **448** (2007) .

[8] E. Laermann and O. Philipsen, "The Status of lattice QCD at finite temperature", *Ann. Rev. Nucl.
Part. Sci.* **53** (2003) , arXiv:hep-ph/0303042.

[9] S. Gupta, X. Luo, B. Mohanty, H. G. Ritter, and N. Xu, "Scale for the Phase Diagram of Quantum
Chromodynamics", *Science* **332** (2011) , arXiv:1105.3934 [hep-ph].

[10] T. Bhattacharya *et al.*, "QCD Phase Transition with Chiral Quarks and Physical Quark Masses",
Phys. Rev. Lett. **113** no. 8, (2014) , arXiv:1402.5175 [hep-lat].

[11] C. Salgado *et al.*, "Proton-Nucleus Collisions at the LHC: Scientific Opportunities and Requirements", *J. Phys. G* **39** (2012) , arXiv:1105.3919 [hep-ph].

[12] K. J. Eskola, P. Paakkinen, H. Paukkunen, and C. A. Salgado, "EPPS16: Nuclear parton distributions with LHC data", *Eur. Phys. J. C* **77** no. 3, (2017) , arXiv:1612.05741 [hep-ph].

[13] **ATLAS** Collaboration, G. Aad *et al.*, "Observation of Long-Range Elliptic Azimuthal Anisotropies in $\sqrt{s}$ =13 and 2.76 TeV *pp* Collisions with the ATLAS Detector", *Phys. Rev. Lett.* **116** no. 17, (2016) , arXiv:1509.04776 [hep-ex].

[14] **ALICE** Collaboration, B. Abelev *et al.*, "Long-range angular correlations on the near and away side in *p*-Pb collisions at $\sqrt{s_{NN}} = 5.02$ TeV", *Phys. Lett. B* **719** (2013) , arXiv:1212.2001 [nucl-ex].

[15] **ALICE** Collaboration, B. B. Abelev *et al.*, "Long-range angular correlations of π, K and p in p-Pb collisions at $\sqrt{s_{NN}} = 5.02$ TeV", *Phys. Lett. B* **726** (2013) , arXiv:1307.3237 [nucl-ex].

[16] **CMS** Collaboration, V. Khachatryan *et al.*, "Evidence for Collective Multiparticle Correlations in p-Pb Collisions", *Phys. Rev. Lett.* **115** no. 1, (2015) , arXiv:1502.05382 [nucl-ex].

[17] **ALICE** Collaboration, S. Acharya *et al.*, "Investigations of Anisotropic Flow Using Multiparticle Azimuthal Correlations in pp, p-Pb, Xe-Xe, and Pb-Pb Collisions at the LHC", *Phys. Rev. Lett.* **123** no. 14, (2019) , arXiv:1903.01790 [nucl-ex].

[18] **ALICE** Collaboration, B. B. Abelev *et al.*, "$K^*(892)^0$ and $\phi(1020)$ production in Pb-Pb collisions at $\sqrt{sNN} = 2.76$ TeV", *Phys. Rev. C* **91** (2015) , arXiv:1404.0495 [nucl-ex].

[19] **ALICE** Collaboration, J. Adam *et al.*, "Multi-strange baryon production in p-Pb collisions at $\sqrt{s_{NN}} = 5.02$ TeV", *Phys. Lett. B* **758** (2016) , arXiv:1512.07227 [nucl-ex].

[20] **ALICE** Collaboration, S. Acharya *et al.*, "Multiplicity dependence of light-flavor hadron production in pp collisions at $\sqrt{s} = 7$ TeV", *Phys. Rev. C* **99** no. 2, (2019) , arXiv:1807.11321 [nucl-ex].

[21] **CMS** Collaboration, V. Khachatryan *et al.*, "Multiplicity and rapidity dependence of strange hadron production in pp, pPb, and PbPb collisions at the LHC", *Phys. Lett. B* **768** (2017) , arXiv:1605.06699 [nucl-ex].

[22] **ALICE** Collaboration, B. B. Abelev *et al.*, "K_S^0 and Λ production in Pb-Pb collisions at $\sqrt{s_{NN}} = 2.76$ TeV", *Phys. Rev. Lett.* **111** (2013) , arXiv:1307.5530 [nucl-ex].

[23] **ALICE** Collaboration, J. Adam *et al.*, "Enhanced production of multi-strange hadrons in high-multiplicity proton-proton collisions", *Nature Phys.* **13** (2017) , arXiv:1606.07424 [nucl-ex].

[24] **ALICE** Collaboration, B. B. Abelev *et al.*, "Multiplicity Dependence of Pion, Kaon, Proton and Lambda Production in p-Pb Collisions at $\sqrt{s_{NN}} = 5.02$ TeV", *Phys. Lett. B* **728** (2014) , arXiv:1307.6796 [nucl-ex].

[25] **ALICE** Collaboration, S. Acharya *et al.*, "Constraints on jet quenching in p-Pb collisions at $\sqrt{s_{NN}}$ = 5.02 TeV measured by the event-activity dependence of semi-inclusive hadron-jet distributions", *Phys. Lett. B* **783** (2018) , arXiv:1712.05603 [nucl-ex].

[26] **ALICE** Collaboration, S. Acharya *et al.*, "Measurements of inclusive jet spectra in pp and central Pb-Pb collisions at $\sqrt{s_{NN}} = 5.02$ TeV", *Phys. Rev. C* **101** no. 3, (2020) , arXiv:1909.09718 [nucl-ex].

[27] **ALICE** Collaboration, S. Acharya *et al.*, "Measurement of charged jet cross section in *pp* collisions at $\sqrt{s} = 5.02$ TeV", *Phys. Rev. D* **100** no. 9, (2019) , `arXiv:1905.02536 [nucl-ex]`.

[28] **ALICE** Collaboration, B. B. Abelev *et al.*, "Charged jet cross sections and properties in proton-proton collisions at $\sqrt{s} = 7$ TeV", *Phys. Rev. D* **91** no. 11, (2015) , `arXiv:1411.4969 [nucl-ex]`.

[29] **ALICE** Collaboration, B. Abelev *et al.*, "Measurement of the inclusive differential jet cross section in *pp* collisions at $\sqrt{s} = 2.76$ TeV", *Phys. Lett. B* **722** (2013) , `arXiv:1301.3475 [nucl-ex]`.

[30] **ALICE** Collaboration, S. Acharya *et al.*, "Charged jet cross section and fragmentation in proton-proton collisions at $\sqrt{s} = 7$ TeV", *Phys. Rev. D* **99** no. 1, (2019) , `arXiv:1809.03232 [nucl-ex]`.

[31] **ALICE** Collaboration, S. Acharya *et al.*, "Constraints on jet quenching in p-Pb collisions at $\sqrt{s_{NN}}$ = 5.02 TeV measured by the event-activity dependence of semi-inclusive hadron-jet distributions", *Phys. Lett. B* **783** (2018) , `arXiv:1712.05603 [nucl-ex]`.

[32] **ALICE** Collaboration, J. Adam *et al.*, "Measurement of dijet k_T in p–Pb collisions at $\sqrt{s_{NN}}$=5.02 TeV", *Phys. Lett. B* **746** (2015) , `arXiv:1503.03050 [nucl-ex]`.

[33] **ALICE** Collaboration, J. Adam *et al.*, "Centrality dependence of charged jet production in p–Pb collisions at $\sqrt{s_{NN}} = 5.02$ TeV", *Eur. Phys. J. C* **76** no. 5, (2016) , `arXiv:1603.03402 [nucl-ex]`.

[34] **ALICE** Collaboration, S. Acharya *et al.*, "Production of Λ and K_S^0 in jets in p-Pb collisions at $\sqrt{s_{NN}} = 5$ TeV and pp collisions at $\sqrt{s} = 7$ TeV", `arXiv:2105.04890 [nucl-ex]`.

[35] T. Sjöstrand, S. Ask, J. R. Christiansen, R. Corke, N. Desai, P. Ilten, S. Mrenna, S. Prestel, C. O. Rasmussen, and P. Z. Skands, "An introduction to PYTHIA 8.2", *Comput. Phys. Commun.* **191** (2015) , `arXiv:1410.3012 [hep-ph]`.

[36] **ALICE** Collaboration, K. Aamodt *et al.*, "The ALICE experiment at the CERN LHC", *Journal of Instrumentation* **3** no. 08, (Aug, 2008) .

[37] **ALICE** Collaboration, B. B. Abelev *et al.*, "Performance of the ALICE Experiment at the CERN LHC", *Int. J. Mod. Phys. A* **29** (2014) , `arXiv:1402.4476 [nucl-ex]`.

[38] **ALICE** Collaboration, E. Abbas *et al.*, "Performance of the ALICE VZERO system", *JINST* **8** (2013) , `arXiv:1306.3130 [nucl-ex]`.

[39] **ALICE** Collaboration, K. Aamodt *et al.*, "Alignment of the ALICE Inner Tracking System with cosmic-ray tracks", *JINST* **5** (2010) , `arXiv:1001.0502 [physics.ins-det]`.

[40] J. Alme *et al.*, "The ALICE TPC, a large 3-dimensional tracking device with fast readout for ultra-high multiplicity events", *Nucl. Instrum. Meth. A* **622** (2010) , `arXiv:1001.1950 [physics.ins-det]`.

[41] **ALICE TOF** Collaboration, A. Akindinov *et al.*, "Particle identification with the ALICE TOF detector at very high particle multiplicity", *Eur. Phys. J. C* **32S1** (2004) .

[42] A. Akindinov *et al.*, "The ALICE Time-Of-Flight system: Construction, assembly and quality tests", *Nuovo Cim. B* **124** (2009) .

[43] A. Akindinov *et al.*, "Results of the ALICE time-of-flight detector from the 2009 cosmic-ray data taking", *Eur. Phys. J. C* **68** (2010) .

[44] **ALICE** Collaboration, F. Carnesecchi, "Performance of the ALICE Time-Of-Flight detector at the LHC", *JINST* **14** no. 06, (2019) , arXiv:1806.03825 [physics.ins-det].

[45] **ALICE** Collaboration, S. Acharya *et al.*, "Production of light-flavor hadrons in pp collisions at $\sqrt{s}$ = 7 and $\sqrt{s}$ = 13 TeV", arXiv:2005.11120 [nucl-ex].

[46] **ALICE** Collaboration, N. Jacazio, "PID performance of the ALICE-TOF detector at Run 2", *PoS* **LHCP2018** (2018) , arXiv:1809.00574 [physics.ins-det].

[47] **ALICE Collaboration** Collaboration, "ALICE luminosity determination for pp collisions at $\sqrt{s} = 13$ TeV",. http://cds.cern.ch/record/2160174.

[48] **ALICE** Collaboration, S. Acharya *et al.*, "Azimuthal correlations of prompt D mesons with charged particles in pp and p–Pb collisions at $\sqrt{s_{NN}}$ = 5.02 TeV", *Eur. Phys. J. C* **80** no. 10, (2020) , arXiv:1910.14403 [nucl-ex].

[49] **ALICE** Collaboration, J. Adam *et al.*, "Pseudorapidity and transverse-momentum distributions of charged particles in proton-proton collisions at $\sqrt{s} = 13$ TeV", *Phys. Lett. B* **753** (2016) , arXiv:1509.08734 [nucl-ex].

[50] M. Cacciari, G. P. Salam, and G. Soyez, "FastJet User Manual", *Eur. Phys. J. C* **72** (2012) , arXiv:1111.6097 [hep-ph].

[51] M. Cacciari, G. P. Salam, and G. Soyez, "The anti-k_t jet clustering algorithm", *JHEP* **04** (2008) , arXiv:0802.1189 [hep-ph].

[52] S. Catani, Y. L. Dokshitzer, M. H. Seymour, and B. R. Webber, "Longitudinally invariant K_t clustering algorithms for hadron hadron collisions", *Nucl. Phys. B* **406** (1993) .

[53] S. D. Ellis and D. E. Soper, "Successive combination jet algorithm for hadron collisions", *Phys. Rev. D* **48** (1993) , arXiv:hep-ph/9305266.

[54] M. Cacciari and G. P. Salam, "Pileup subtraction using jet areas", *Phys. Lett. B* **659** (2008) , arXiv:0707.1378 [hep-ph].

[55] M. Cacciari, G. P. Salam, and G. Soyez, "The Catchment Area of Jets", *JHEP* **04** (2008) , arXiv:0802.1188 [hep-ph].

[56] **CMS** Collaboration, S. Chatrchyan *et al.*, "Measurement of the underlying event activity in *pp* collisions at $\sqrt{s} = 0.9$ and 7 TeV with the novel jet-area/median approach", *JHEP* **08** (2012) , arXiv:1207.2392 [hep-ex].

[57] **ALICE** Collaboration, J. Adam *et al.*, "Measurement of charged jet production cross sections and nuclear modification in p-Pb collisions at $\sqrt{s_{NN}}$ = 5.02 TeV", *Phys. Lett. B* **749** (2015) , arXiv:1503.00681 [nucl-ex].

[58] **ALICE** Collaboration, J. Adam *et al.*, "Centrality dependence of charged jet production in p–Pb collisions at $\sqrt{s_{NN}}$ = 5.02 TeV", *Eur. Phys. J. C* **76** no. 5, (2016) , arXiv:1603.03402 [nucl-ex].

[59] **Particle Data Group** Collaboration, M. Tanabashi *et al.*, "Review of Particle Physics", *Phys. Rev. D* **98** (Aug, 2018) .

[60] **ALICE** Collaboration, K. Aamodt *et al.*, "Strange particle production in proton-proton collisions at sqrt(s) = 0.9 TeV with ALICE at the LHC", *Eur. Phys. J. C* **71** (2011) , `arXiv:1012.3257 [hep-ex]`.

[61] **ALICE** Collaboration, B. Abelev *et al.*, "Multi-strange baryon production in *pp* collisions at $\sqrt{s} = 7$ TeV with ALICE", *Phys. Lett. B* **712** (2012) , `arXiv:1204.0282 [nucl-ex]`.

[62] **ALICE** Collaboration, S. Acharya *et al.*, "Multiplicity dependence of (multi-)strange hadron production in proton-proton collisions at $\sqrt{s} = 13$ TeV", *Eur. Phys. J. C* **80** no. 2, (2020) , `arXiv:1908.01861 [nucl-ex]`.

[63] S. Roesler, R. Engel, and J. Ranft, "The Monte Carlo event generator DPMJET-III", in *International Conference on Advanced Monte Carlo for Radiation Physics, Particle Transport Simulation and Applications (MC 2000)*, pp. 1033–1038. 12, 2000. `arXiv:hep-ph/0012252`.

[64] R. Brun, F. Bruyant, F. Carminati, S. Giani, M. Maire, A. McPherson, G. Patrick, and L. Urban, "GEANT Detector Description and Simulation Tool",.

[65] **ALICE** Collaboration, J. Adam *et al.*, "Multi-strange baryon production in p-Pb collisions at $\sqrt{s_{\mathrm{NN}}} = 5.02$ TeV", *Phys. Lett. B* **758** (2016) , `arXiv:1512.07227 [nucl-ex]`.

[66] **ALICE** Collaboration, J. Adam *et al.*, "Multiplicity dependence of charged pion, kaon, and (anti)proton production at large transverse momentum in p-Pb collisions at $\sqrt{s_{\mathrm{NN}}} = 5.02$ TeV", *Phys. Lett. B* **760** (2016) , `arXiv:1601.03658 [nucl-ex]`.

[67] **ALICE** Collaboration, B. B. Abelev *et al.*, "Multiplicity Dependence of Pion, Kaon, Proton and Lambda Production in p-Pb Collisions at $\sqrt{s_{NN}} = 5.02$ TeV", *Phys. Lett. B* **728** (2014) , `arXiv:1307.6796 [nucl-ex]`.

A Particle candidate selection criteria

Table A.1: K_S^0 (Λ and $\overline{\Lambda}$) candidate selection criteria of topological variables, daughter tracks and V^0 candidates. The DCA stands for the "Distance of Closest Approach", PV represents the "Primary collision Vertex" and CPA is the "Cosine Pointing Angle between the momentum vector of the reconstructed V^0 and the displacement vector between the decay and primary vertices".

Topological variable	pp	p–Pb
V^0 transverse decay radius	> 0.5 cm	> 0.5 cm
DCA of positive / negative track to PV	> 0.06 cm	> 0.06 cm
DCA between V^0 daughter tracks	$< 1.0\sigma$	$< 1\sigma$
CPA of V^0	> 0.97 (0.995)	> 0.97 (0.995)
Track selection		
Daughter track pseudo-rapidity interval	$|\eta| < 0.8$	$|\eta| < 0.8$
Daughter track $N_{\text{crossed rows}}$	≥ 70	≥ 70
Daughter Track $N_{\text{crossed rows}}/N_{\text{findable}}$	≥ 0.8	≥ 0.8
TPC dE/dx	$< 5\sigma$	$< 5\sigma$
Candidate selection		
Pseudo-rapidity interval	$|\eta| < 0.75$	$|\eta| < 0.75$
Proper lifetime (mL/p)	< 20 (30) cm	< 20 (30) cm
Competing mass	> 0.005 (0.010) GeV/c^2	> 0.005 (0.010) GeV/c^2

Table A.2: $\Xi^{\pm}$ ($\Omega^{\pm}$) candidate selection criteria of topological variables, daughter tracks and cascade candidates.

Topological variable	pp	p–Pb
Cascade transverse decay radius	$> 0.8(0.6)$ cm	> 0.6 cm
V^0 transverse decay radius	> 1.4 cm	> 1.2 cm
DCA (bachelor to PV)	> 0.05 cm	> 0.04 cm
DCA (V^0 to PV)	> 0.07 cm	> 0.06 cm
DCA (positive / negative track to PV)	$> 0.04(0.03)$ cm	> 0.03 cm
DCA between V^0 daughter tracks	$< 1.6\sigma$	$< 1.5\sigma$
DCA (bachelor to V^0)	$< 1.6(1.0)$ cm	< 1.3 cm
CPA of Cascade	> 0.97	> 0.97
CPA of V^0	> 0.97	> 0.97
V^0 invariant mass window	± 0.006 GeV/c^2	± 0.008 GeV/c^2
Track selection		
Daughter track pseudo-rapidity interval	$|\eta| < 0.8$	$|\eta| < 0.8$
Daughter track $N_{\text{crossed rows}}$	≥ 70	≥ 70
Daughter Track $N_{\text{crossed rows}}/N_{\text{findable}}$	≥ 0.8	≥ 0.8
TPC dE/dx	$< 5\sigma$	$< 4\sigma$
Candidate selection		
Pseudo-rapidity interval	$|\eta| < 0.75$	$|\eta| < 0.75$
Proper lifetime (mL/p)		$< 3 \times c\tau$
Competing mass	8 MeV/c^2	8 MeV/c^2

460 **B The ALICE Collaboration**